Supplementary Note 1

Quantitative Analysis Information

This document contains the following sections:

1. Cell fate imbalance

To assess potential changes in cell fate during postnatal development, we can make an estimate of the evolving fate imbalance by combining morphometric measures and proliferation kinetics. If we assume that the basal cell population constitutes a single, equipotent, proliferative compartment, then the change in basal cell number, B, can be parameterized through the stochastic process,

$$B \xrightarrow{\lambda} \begin{cases} B + B & \textbf{Probability } (1 + f)/2 \\ S & \textbf{Probability } (1 - f)/2 \end{cases}$$

where stratification of cells into the suprabasal layer (S) leads to basal cell loss, λ denotes an "effective" cell proliferation rate and f denotes the degree of fate imbalance. Based on clonal fate studies, evidence in support of such a model has been provided in Doupe et al. 2012 in the context of tissue homeostasis[1]. When $f = 0$, the basal cell number remains constant over time while, for $f > 0$, there is a tilt towards cell duplication leading to a net expansion of the basal cell number. Based on this definition, the differential change in basal cell number is then given by

$$\frac{\dot{B}}{B} = f\lambda$$

where $\dot{B}$ denotes the time derivative of B, and both f and λ can, and do, change over time. Since we can estimate both the differential change in basal cell number through measurements of the basal cell density and the total area of the tissue, and the division rate based on short-term EdU incorporation, we can access the degree of fate imbalance as

$$f = \frac{1}{\lambda}\frac{\dot{B}}{B}$$

More precisely, for time point i, we set $\dot{B}_i \equiv (B_i - B_{i-1})/(t_i - t_{i-1})$, and $\lambda_i \equiv ((E_i - E_{i01})/E_0)\lambda_0$, with E_i the percentage of EdU positive cells following a short-term pulse (2h) and the values of E_0 and λ_0, used for normalization, are obtained from steady-state homeostasis[1].

Note that, although this quantity is well-defined based on the experimental measurements, it's interpretation as a measure of fate imbalance could be compromised if the basal cell compartment were heterogeneous. In particular, if the basal compartment included a fraction of cells already committed to terminally differentiation, this measure of f could underestimate the actual degree of fate imbalance. However, based on our EdU incorporation data, we find evidence that basal cells can commit to differentiation soon after division, pointing to a short residency time in the basal cell layer. Moreover, since any changes in the basal cell composition are likely to take place on a slow time scale, our estimate for f can be safely used as a qualitative, if not quantitative, measure of the changes in fate imbalance during the postnatal period.

2. KLF4 marks progenitor commitment from post-mitotic stages

We next took advantage of the basal KLF4 expression, marking early differentiation, to investigate an open and contested question in the squamous epithelial field. It is debated as to whether basal progenitors initiate commitment toward differentiation from the moment of division, or whether cell fate outcome is assigned later, following a refractory period in the basal compartment[1-6]. We explored this question by comparing the expression of KLF4 in post-mitotic EdU basal pairs, as marked by a 12h EdU chase[7] (**Fig. 2l,m**), with the division outcomes predicted by our previous model of oesophageal cell dynamics[1] (**Fig. 2n;** Doupe et. al. model between parentheses). In this model, oesophageal progenitors divide stochastically choosing at random between one of three possible fate outcomes; generating two daughters that will go on to divide (symmetric division, 10%), two cells

that will exit cycle and eventually differentiate (symmetric differentiation, 10%), or one of each fate (asymmetric division, 80%). Our results revealed KLF4 levels being reliably detected in EdU+ sister cells just hours after their physical post-mitotic separation. Quantitative analysis showed that the majority of divided cell pairs were localized to the basal layer, and either remained KLF4- (~43%), or exhibited one KLF4+ cell (~40%). The rest of the pairs (~17%) showed both nuclei bright for KLF4 (**Fig. 2n,o**). Very rarely, an EdU+ pair presented one sister localized in the immediate suprabasal layer (7 out of 150 pairs; ~5%), in which case the suprabasal cell was always KLF4+. Our pair analysis indicated that a marked fraction of cells acquire KLF4 expression at the cell division stage, supporting the notion that fate can be assigned from the time of division. Interestingly, asymmetric KLF4 pairs (40%) only accounted for half of the asymmetric divisions predicted by the model (80%), suggesting an active process where commitment continues beyond the division stage.

This data provides further insight into the temporal resolution of cell fate commitment. In particular, it reveals that commitment towards differentiation can be defined from the division stage, without the need for a refractory period in the basal layer. Further, we propose a progressive commitment process, where progenitor cells retain a degree of flexibility in their fate outcome to face specific tissue needs and challenges.

3. Quantitative image analysis of tissue architecture.

3.1. Tissue image segmentation

Prior to analysis, all microscopy images were converted into 8 bit TIF files from their native proprietary file format. In addition to immunostainings of interest, DAPI and Phalloidin were used to label nuclei and cell contours, respectively, in wholemounts and sections of the oesophageal epithelium (OE). Nuclei and cell contours were then segmented, using an automated deep learning based image segmentation framework coded in Python, based mainly on Keras and TensorFlow libraries, and described in greater details elsewhere (A. Hallou et al., unpublished).

For each experiment, a "training" image set of four to six representative images was selected for each time point, with images taken from at least three biological replicates. A "ground truth" segmentation mask was obtained for each image of the training set using a semi-automated pipeline based on "ilastik", a random forest classifier-based machine learning library for image segmentation[8]. For each condition, the random forest classifier was trained to distinguish between background and foreground pixels of interest producing a probability map of the image of interest, giving each pixel a particular probability to belong to a given class (background or foreground). A binary mask of the image was then obtained using a thresholding of the probability map, followed by post-processing steps composed of morphological opening/closing operations, size filtering and manual corrections.
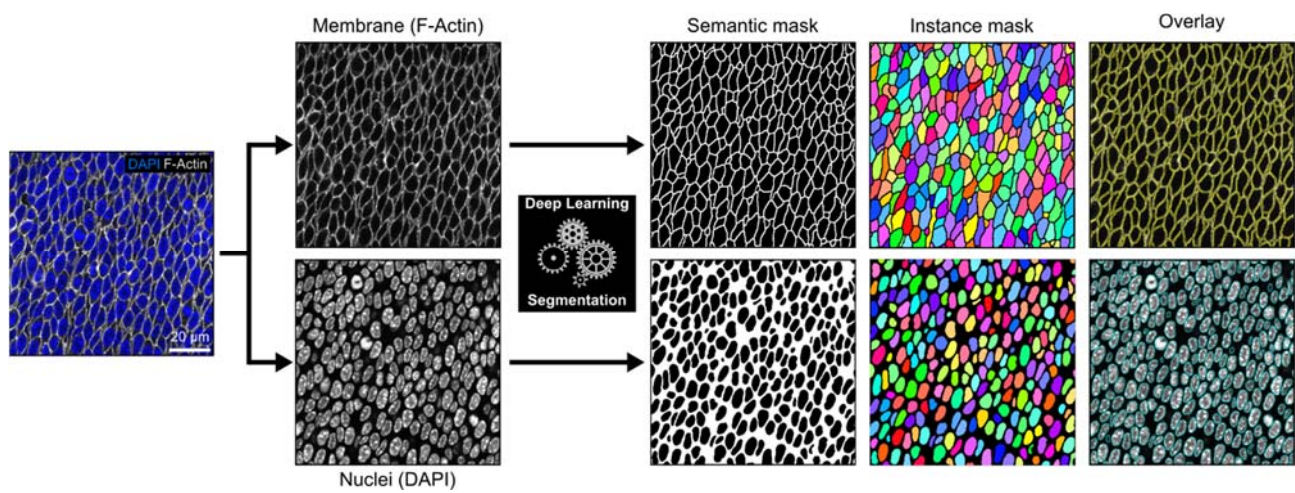
Supplemental Information Figure 1: Deep learning based segmentation of nuclei and cell membrane. Schematic of the application of the deep learning based image segmentation pipeline to segment cell nuclei and membranes on single z confocal slices of the basal layer of the esophageal epithelium stained with DAPI (nuclei, blue) and Phalloidin (F-Actin, grey). The different panels show the semantic (binary) and instance segmentation masks obtained as outputs of the pipeline and an overlay of the binary masks on the original fluorescence images. The overlay mask for the membrane was used to measure the intensity of the F-Actin fluorescence signal.

To achieve full automation of image segmentation, we adopted a deep learning approach based on U-Net networks, a family of convolutional neural networks with an encoder/decoder architecture recently used for a variety of computer vision tasks, including biological and medical image analysis[8]. As shown in **Extended Data Fig. 5c**, we trained our U-Net network for each experiment using the training image set and associated ground truth binary masks prepared at the previous step. Training images were first subdivided into two groups; a first group containing two-thirds of the images was used to train the network, while a second group, composed of the remaining images, was used for training validation.

Training was performed at original image resolution and image intensity was normalised between 0 and 1. Random rotation and elastic deformation were used as image augmentation techniques. The "loss function" used for training was pixel-weighted binary cross-entropy, with weighting used to

4

enforce instance separation and class-balance (background vs. foreground objects). For initial training, the loss function was minimised on the training set using a stochastic gradient descent algorithm at a basal learning rate of 10^{-4} with a first momentum of 0.9 and second momentum of 0.999 for around 2.0-3.0 x 10^5 time-steps until reaching a learning rate decay of less than 10^{-4} for more than 10^4 time-steps. Performance of the training was assessed on validation images using mean intersection over union (IoU) as a main metric for semantic segmentation accuracy, and was iteratively optimised until an IoU>93±3% was achieved for all training image sets.

Once the network was trained, other images of the same experiment were processed automatically to obtain binary nuclear and membrane masks, (as illustrated **in Supplemental Information Fig. 1**). Instance objects, i.e. individual nuclei or cells, were subsequently identified using a seeded watershed algorithm, using the ultimate points of binary mask as seeds[9].

3.2. Pipeline to analyse the spatial organisation and morphological properties of basal cells

Using the instance mask of each image, 20 different individual spatial and morphological properties of each nucleus or cell were systematically extracted: 1, surface area; 2, centroid x position; 3, centroid y position; 4, perimeter; 5, bounding box centre x position; 6, bounding box centre y position; 7, bounding box width; 8, bounding box height; 9, ellipse major axis; 10, ellipse minor axis; 11, ellipse major axis angle (with image x axis); 12, circularity; 13, Feret diameter; 14, Feret x start position; 15, Feret y start position; 16, Feret angle (with image x axis); 17, minimum Feret diameter; 18, aspect ratio; 19, Roundness and 20, Solidity. Generated data were stored in individual CSV files and subsequently analysed using custom Python scripts.

The point configuration made by the ensemble of nuclear centroids was used as the start point for further analysis of the tissue spatial organisation as shown in **Extended Data Fig. 5e**.

The basal cell density, ρ, was evaluated as the average number of centroid points, N, per surface area, L^2, in 2D single-plane images of the OE basal layer:

$$\rho = \left\langle \frac{N}{L^2} \right\rangle$$

where $\langle .. \rangle$ denotes an average over all cells in the image. From this result, we obtained the characteristic neighbour distance between basal cells,

$$l_c = \frac{1}{\sqrt{\rho}}$$

5

To further quantify the spatial organisation of tissue, the bidimensional structure factor, $S(\boldsymbol{k})$ was derived, which characterises the long-range spatial organisation of the tissue:

$$S(\boldsymbol{k}) = \frac{1}{N}\left|\sum_{j=1}^{N} exp\left(i\boldsymbol{k} \cdot \boldsymbol{r}_j\right)\right|^2$$

Here $\boldsymbol{r}_j$ denote centroid position vectors of nuclei and $\boldsymbol{k} = \begin{pmatrix} k_x \\ k_y \end{pmatrix}$ is the wave vector[10]. For practical purposes, the non-physical "forward scattering" contribution ($\boldsymbol{k} = 0$) was excluded, and $\boldsymbol{k}$ was computed using periodic boundary conditions, which is a reasonable assumption given that L is much smaller than the overall tissue size:

$$k_x = k_y = \frac{2\pi n}{L}(n \in \mathbb{N}).$$

The values taken by the structure factor at small wave numbers reflect the degree to which there exists a large-scale spatial organisation of cells in the tissue and thus, if the tissue possesses positional order, $S(\boldsymbol{k})$ should significantly deviate from unity when $\mathbf{k}$ is small[11]. The structure factor anisotropy was then derived to quantify the extent to which the tissue spatial organisation varies along the different spatial coordinates[12]. To do so, the bidimensional structure factor was thresholded such that only values well below unity were kept:

$$\bar{S}(\boldsymbol{k}) = S(\boldsymbol{k}) \lessapprox 1.0.$$

The shape anisotropy tensor of the thresholded structure factor, $\bar{S}(\boldsymbol{k})$, could then be derived as:

$$\boldsymbol{I}_{\bar{S}} = \begin{pmatrix} \langle k_x k_x \rangle & \langle k_x k_y \rangle \\ \langle k_x k_y \rangle & \langle k_y k_y \rangle \end{pmatrix}$$

where k_x and k_y are now the coordinates of all the points of the thresholded structure factor with their origin taken at their barycentre $\langle k_x \rangle = \langle k_x \rangle = 0$, with brackets indicating an average over space. The four terms that appear in $\boldsymbol{I}_{\bar{S}}$ represent the coordinate covariances. From the eigenvalues of $\boldsymbol{I}_{\bar{S}}$, λ_1 and λ_2, one can obtain the anisotropy of the structure factor as:

$$A_{\mathrm{SF}} = \frac{\lambda_1 - \lambda_2}{\sqrt{\lambda_1^2 + \lambda_2^2}}.$$

From the coordinates of nuclei centroids, it is also possible to retrieve Voronoi diagrams of the epithelial tissue as the dual of their Delaunay triangulation[13]. We used the standard Delaunay triangulation algorithm provided by the SciPy library, but calculated modified Voronoi diagrams to handle infinite cells at the boundary of the image as shown in **Extended Data Fig. 5e**. Voronoi diagrams were not used as a realistic representation of the tissue, but as a means to quantify the

local topology of the tissue; and also as a convenient way to display various measured quantities that were colour-mapped onto them.

It is possible to carry out a similar analysis of the spatial organisation of the tissue at the individual cell level. Indeed, from the knowledge of the coordinates of every segmented cell outline, it was possible to derive the cellular shape anisotropy tensor:

$$I_c = \begin{pmatrix} \langle xx \rangle & \langle xy \rangle \\ \langle xy \rangle & \langle yy \rangle \end{pmatrix}$$

where x and y are now the coordinates of all the points of the cell contour with their origin taken at their barycentre $\langle x \rangle = \langle y \rangle = 0$ (i.e. at the cell centroid), with brackets indicating an average over space. From the eigenvalues of I, λ_1 and λ_2, we can obtain the cell shape anisotropy A_c:

$$A_c = \frac{\lambda_1 - \lambda_2}{\sqrt{\lambda_1^2 + \lambda_2^2}}$$

The determination of the eigenvectors, allowed determination of the orientation of the long axis, θ, and short axis, which is perpendicular to it. Also, knowing λ_1, λ_2 and θ, one can represent the shape anisotropy tensor of each cell as an ellipse centred at its centroid and whose orientation is given by θ, and long and short axis lengths by λ_1 and λ_2 respectively.

Following the Landau-De Gennes theory of liquid crystals, the distribution of orientation of the long axis of each cell can also be used to quantify the orientational order of cells in the tissue, defining an orientation tensor[14]:

$$O = \begin{pmatrix} \langle \cos\theta^2 \rangle & \langle \cos\theta \sin\theta \rangle \\ \langle \cos\theta \sin\theta \rangle & \langle \sin\theta^2 \rangle \end{pmatrix}$$

Basic linear algebra allows determination of the dominant eigenvalue of O, which is called the nematic order parameter,

$$S = \sqrt{\langle \cos\theta^2 \rangle + \langle \sin\theta^2 \rangle}$$

This quantity is averaged over all segmented cells in an image and is thus a readout of the average orientational order in the tissue. The limiting case *S=0* would describe a completely disordered tissue, where cellular orientations are uncorrelated, while the limiting case *S=1*, would describe a perfect nematic order where all cells align with their neighbours[15].

3.3. Analysis-Transition to homeostasis coincides with spatial tissue reorganization

An initial qualitative analysis revealed considerable changes in basal cell morphology, density and spatial organization of the tissue (**Fig. 4a-c**). Specifically, at early time points (P7 and P14), when proliferative activity is at its highest (**Fig. 1e-g**), basal cells were tightly packed, as shown by their higher cell density relative to later time points (**Fig. 4c**). We next used the deep learning image segmentation analysis pipeline described above to precisely analyse changes in the architecture of the postnatal OE (**Extended Data Fig. 5c-e**). At early stages, basal cells exhibit increased shape anisotropy, being markedly elongated along the anterior-posterior longitudinal axis of the oesophagus (**Fig. 4d and Extended Data Fig. 5f,g**). This spatial anisotropy was also observed at the tissue level, as evidenced by changes in the bidimensional structure factor of the OE (**Fig. 4e and Extended Data Fig. 5h,i;** see Methods). This data suggests that the increased cellular crowding and associated mechanical stress experienced by the highly proliferative OE at P7 and P14 favours the spatial order and orientational alignment of cells. This notion was supported by higher values of the nematic order parameter, which measures the average orientational order of cells in the tissue, at early postnatal stages (P7-14; **Fig. 4f;** see Methods). Alignment of densely packed cells was indeed consistent with previous *in vitro* and *in vivo* work[16-18]. In line with observations made throughout this study, the anisotropic pattern and long-range orientational alignment of basal cells became less apparent from P28 onwards, when most homeostatic features establish (**Fig. 4d-f and Extended Data Fig. 5f-i**). Our data reveals how changes in the physical parameters that define epithelial tissue organization correlate with the physiological processes engineering the switch from postnatal expansion to homeostasis in the OE.

3.4. Second harmonic generation pipeline

Second Harmonic Generation (SHG) signals allow imaging of the collagen contained in the stromal compartment of the oesophagus in a label-free fashion. We analysed the spatial organisation of this essential extracellular matrix component in single-plane images taken from z-stacks acquired immediately below the OE basement membrane.

To extract the local orientation of collagen fibres in these images, we followed an approach based on the image structure tensor[19]. This quantity is defined for all pixels in an image as:

$$J = \begin{pmatrix} \langle \partial_x I(x,y),\, \partial_x I(x,y) \rangle_w & \langle \partial_x I(x,y)\,,\partial_y I(x,y) \rangle_w \\ \langle \partial_x I(x,y), \partial_y I(x,y) \rangle_w & \langle \partial_y I(x,y), \partial_y I(x,y) \rangle_w \end{pmatrix}$$

where $I(x,y)$ is the image intensity and $\langle f, g \rangle_w = \iint w(x,y) f(x,y) g(x,y)\, dx\, dy$ is the convolution by a 2D Gaussian kernel $w(x,y)$ of width σ. Using basic linear algebra, it is possible to determine the

eigenvalues and eigenvectors of this tensor, and to define the local dominant orientation θ as the direction of the largest eigenvector of $\boldsymbol{J}$:

$$\theta = \frac{1}{2}\tan^{-1}\left(2\frac{\langle \partial_x I(x,y),\, \partial_y I(x,y)\rangle_w}{\langle \partial_y I(x,y),\, \partial_y I(x,y)\rangle_w - \langle \partial_x I(x,y),\, \partial_x I(x,y)\rangle_w}\right)$$

In practice, we used a 2D Gaussian kernel of $\sigma = 6$ pixels width, and the values obtained for θ were locally averaged on a grid with a mesh size of 20 pixels in order to cancel out local variability due to intensity variation and edge effects.

The collagen fibre orientation distributions obtained this way (**Extended Data Fig. 6h**) were averaged over at least 3 technical replicates per biological replicate, and data from at least 3 biological replicates per time point were used to plot angular distribution histograms shown in **Extended Data Fig. 6i**. We also characterised for each time point the dominant orientation, the standard deviation of the orientation, and the orientational order parameter of collagen fibre Q. This quantity is defined, from the mathematical standpoint, in a similar fashion to the nematic order parameter i.e. as the dominant eigenvalue of the orientation tensor $\boldsymbol{O}$:

$$Q = \sqrt{\langle \cos\theta^2\rangle + \langle \sin\theta^2\rangle}.$$

The physical interpretation of this quantity is also similar even if its biophysical origin or the space scales involved are completely different.

3.5. Analysis- Second harmonic generation

The ECM constitutes an important factor for tissue mechanics, representing the scaffolding over which epithelial cells are sustained[20]. Second harmonic generation (SHG) imaging revealed an active remodelling of ECM structural components during oesophageal development (**Extended Data Fig. 6h**), in line with the ECM signature identified by scRNA-seq (**Extended Data Fig. 4b**). Quantitative analysis showed that the ECM mesh at P7 consists of a wide range of fibre orientations (**Extended Data Fig. 6h,i;** top panels). This profile is lost by P28, when fibres become aligned transverse to the oesophageal tube (**Extended Data Fig. 6h,i**), which may represent a mechanism to dissipate part of the tensile load of the tissue along its longitudinal axis.


3.6. Analysis of F-Actin expression levels

To quantify cortical F-Actin expression levels on the basis of the Phalloidin fluorescence signal (**Figure 5g**), the semantic mask of cell contours obtained through our deep learning segmentation pipeline was used. For each image, this binary mask was submitted to a series of morphological

operations to extract a "skeleton" mask of cell contours. This skeleton mask was then uniformly dilated by 2 pixels in order to obtain a mask to be used for measuring the cortical Phalloidin fluorescence intensity. The mean pixel fluorescence intensity over the masked region of each image was computed, and its average and standard deviation over technical and biological replicates used as a readout of F-Actin expression levels and variability (**Figure 5i**).

3.7. Analysis of active Myosin II levels

To quantify levels of active Myosin II in cells of the basal layer of the oesophageal epithelium, confocal images of transversal sections of the oesophagus stained for phosphorylated myosin light chain II (pMLC2) and nuclear DAPI were used (**Figure 5h)**. Our deep learning segmentation pipeline was implemented to segment cell nuclei and regions of the tissue stained for pMLC2. Using the semantic segmentation masks obtained for both tissue regions and additional filtering and morphological operations, it was possible to delineate accurate instance masks for the stroma, basal layer of the epithelium and suprabasal layer of the epithelium. These regional instance masks obtained for each image were then used to measure the pMLC2 fluorescence intensity (**Supplemental Information Fig. 2**). The mean pixel fluorescence intensity over the masked regions of each image was computed, and its average and standard deviation over technical and biological replicates used as a readout of active myosin II levels and variability (**Fig. 5j**).
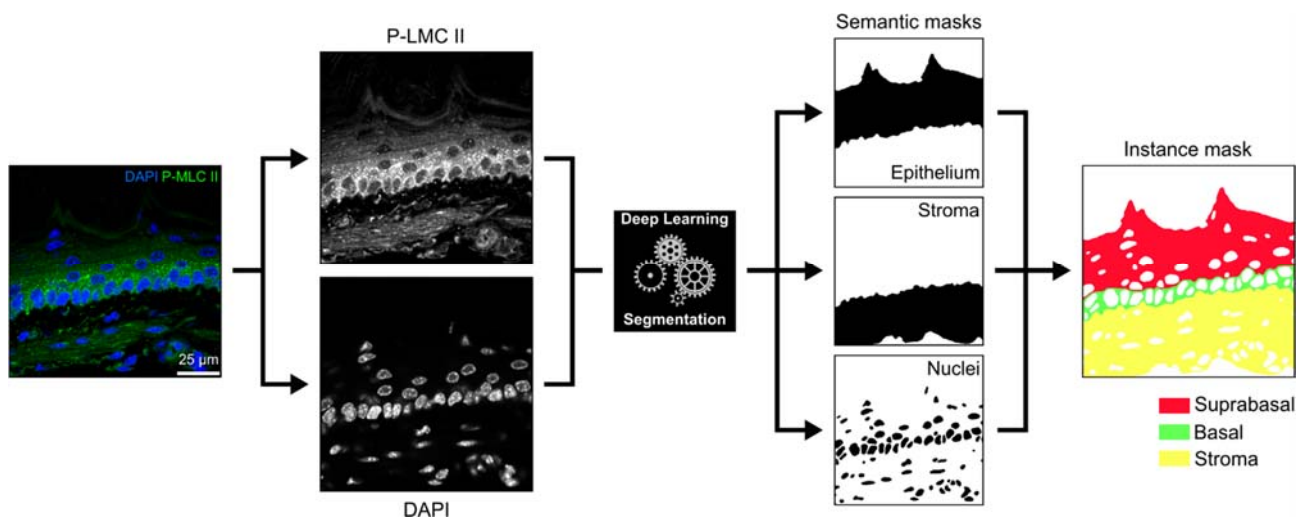
Supplemental Information Figure 2: Determination of active Myosin II levels. Schematic of the application of the deep learning based image segmentation pipeline to the segmentation of cell nuclei and tissue layers (stroma, epithelial basal and suprabasal layers) on single z-slice confocal images of sections of the esophagus stained with DAPI (nuclei, blue) and immunostained for Phospho-Myosin Light Chain II (pMLC2, green). Instance masks for the different tissue layers were obtained from the semantic masks using a combination of filters and common morphological operations. Instance mask for the basal layer was used to measure the intensity of the pMLC2 fluorescence signal.

4. Differential growth promotes longitudinal strain in the oesophagus

To explore whether the oesophagus grows at a similar rate than the rest of the body, we measured the length of this organ before (*in situ*) and after dissection (*ex vivo*), and compared it to the mouse body length at different postnatal time points from P7 up to adulthood (**Fig. 5a,b and Extended Data Fig. 6a**). Lengths were all expressed as a percentage relative to their value at P7 (**Fig. 5c**). Naturally, the length of the *in situ* oesophagus and entire body showed an almost perfect overlap. Intriguingly, the *ex vivo* length, when detached from any adjacent tissues, did not follow the same trend. When approaching P28, the length of the *ex vivo* oesophagus increased at a seemingly slower pace than the rest of the body, resulting in a 30% longitudinal strain by adulthood (**Fig. 5d**). We confirmed that the observed discrepancy in length was not an artefact imposed by the underlying muscle layer by measuring the length of the muscle compartment independently. Interestingly, we found that the muscle layer was approximately 10% longer than the adult *ex vivo* OE, adding a further 10% to the longitudinal strain of the adult epithelium (**Extended Data Fig. 6b,c**). Therefore, the differential growth of the developing oesophagus results in the build-up of a progressive strain, estimated to be between 20% and 40% from P28 to adult, under normal physiological conditions.

5. Link between YAP and KLF4 basal cell expression

To explore a potential link between YAP and KLF4 in the basal cell compartment, we used three different approaches. First, we co-stained and quantified the levels of both proteins in the nucleus of adult basal cells (**Fig. 6a-c**). This data confirms a positive correlation between YAP and KLF4; with cells in the top 20th percentile of nuclear YAP expression having significantly higher levels of KLF4 (**Fig. 6b-c**). Second, we looked at KLF4 expression upon interfering with YAP signalling *in vivo*. For this, we used an inducible mouse line (Krt5-rtTA;TEADi [21]), where the expression of a dominant negative form of the YAP co-activator TEAD is under the control of doxycycline. Genetic induction results in the blockage of YAP- and TAZ-induced TEAD activity in the basal cell compartment. After chasing adult mice with doxycycline for 3 weeks, KFL4 was quantified in TEADi+ and TEADi- basal cells, as detected by the TEADi associated GFP reporter. The results show that TEADi+ cells present reduced expression of KLF4, while being enriched for the proliferation marker Ki67 (**Fig. 6d-f**). Third, we further tested this idea by investigating the impact of YAP overactivation in the early postnatal OE, when basal cells are still negative for KLF4 (**Fig. 2a,b,g**). For this, we used the YAPS127A Doxycycline (Dox) inducible mouse strain R26-rtTA;tetO-YAPS127A (rtTA/tetOYAP). P6 rtTA/tetOYAP mice were Dox treated for 72h and the OE collected to analyse KLF4 expression in the basal layer (**Fig. 6g**). Tissue sections of the same samples indicated the presence of nuclear YAP staining in P6 induced animals as opposed to littermate non-induced controls, confirming the

exogenous YAPS127A expression (**Fig. 6h**). In line with our prediction, we detected a significant increase in basal KLF4 levels upon YAPS127A induction (**Fig. 6i,j**). This experiment also denoted YAPS127A+/KLF4+ double positive cells departing from the basal compartment, and starting the journey towards differentiation (**Fig. 6h**), which resulted in an expanded KLF4 suprabasal compartment in rtTA/tetOYAP P9 mice compared to controls (**Fig. 6k**).

Collectively, co-localization experiments as well as *in vivo* YAP activating and inhibiting mouse models demonstrated that increased YAP nuclear localization promotes KLF4 expression in the basal cell compartment, balancing progenitor cell behaviour through commitment.

6. Adult oesophageal keratinization provides structural integrity

It was interesting to observed that *in vitro* BLEBB treatment did not only led to a reduction in basal cell area in stretched adult tissue, but also in unstretched controls to a more modest degree (**Extended Data Fig. 7c,d;** 0% controls unstretched). The nature of the squamous oesophagus provides clues to anticipate this result. A key difference of the adult oesophagus, when compared to earlier time points, is the presence of a fully keratinized/cornified suprabasal compartment (**Extended Data Fig. 1 j,k**), known to provide structural support[22, 23]. The notion that tissue keratinization serves as a means to preserve mechanical features in the matured oesophagus was assessed by experiments where the upper suprabasal layers that delimit the epithelium were physically separated (**Extended Data Fig. 7e**). As anticipated, removal of highly keratinized layers resulted in a significant reduction in basal cell area (**Extended Data Fig. 7e-g**). Stromal detachment provided similar observations, suggesting that the composite of layers that delimit the adult epithelium help retain its structural integrity.

References

1. Doupe, D.P. *et al.* A single progenitor population switches behavior to maintain and repair esophageal epithelium. *Science* **337**, 1091-1093 (2012).
2. Mesa, K.R. *et al.* Homeostatic Epidermal Stem Cell Self-Renewal Is Driven by Local Differentiation. *Cell Stem Cell* **23**, 677-686 e674 (2018).
3. Rompolas, P. *et al.* Spatiotemporal coordination of stem cell commitment during epidermal homeostasis. *Science* **352**, 1471-1474 (2016).
4. Kulukian, A. & Fuchs, E. Spindle orientation and epidermal morphogenesis. *Philos Trans R Soc Lond B Biol Sci* **368**, 20130016 (2013).
5. Clayton, E. *et al.* A single type of progenitor cell maintains normal epidermis. *Nature* **446**, 185-189 (2007).
6. Mascre, G. *et al.* Distinct contribution of stem and progenitor cells to epidermal maintenance. *Nature* **489**, 257-262 (2012).
7. Alcolea, M.P. *et al.* Differentiation imbalance in single oesophageal progenitor cells causes clonal immortalization and field change. *Nat Cell Biol* **16**, 615-622 (2014).
8. Berg, S. *et al.* ilastik: interactive machine learning for (bio)image analysis. *Nat Methods* **16**, 1226-1232 (2019).
9. Legland, D., Arganda-Carreras, I. & Andrey, P. MorphoLibJ: integrated library and plugins for mathematical morphology with ImageJ. *Bioinformatics* **32**, 3532-3534 (2016).
10. Hansen, J.-P. & McDonald, I.R. *Theory of simple liquids : with applications of soft matter*, Edn. Fourth edition. (Elsevier/AP, Amsterdam; 2013).
11. Chen, D., Aw, W.Y., Devenport, D. & Torquato, S. Structural Characterization and Statistical-Mechanical Model of Epidermal Patterns. *Biophys J* **111**, 2534-2545 (2016).
12. Durande, M. *et al.* Fast determination of coarse-grained cell anisotropy and size in epithelial tissue images using Fourier transform. *Phys Rev E* **99**, 062401 (2019).
13. Kaliman, S., Jayachandran, C., Rehfeldt, F. & Smith, A.S. Limits of Applicability of the Voronoi Tessellation Determined by Centers of Cell Nuclei to Epithelium Morphology. *Front Physiol* **7**, 551 (2016).
14. Gennes, P.G.d. & Prost, J. *The physics of liquid crystals*, Edn. 2nd. (Clarendon Press ; Oxford University Press, Oxford New York; 1993).
15. Duclos, G., Garcia, S., Yevick, H.G. & Silberzan, P. Perfect nematic order in confined monolayers of spindle-shaped cells. *Soft Matter* **10**, 2346-2353 (2014).
16. Saw, T.B. *et al.* Topological defects in epithelia govern cell death and extrusion. *Nature* **544**, 212-216 (2017).
17. Kawaguchi, K., Kageyama, R. & Sano, M. Topological defects control collective dynamics in neural progenitor cell cultures. *Nature* **545**, 327-331 (2017).
18. Morales-Navarrete, H. *et al.* Liquid-crystal organization of liver tissue. *Elife* **8** (2019).
19. Rezakhaniha, R. *et al.* Experimental investigation of collagen waviness and orientation in the arterial adventitia using confocal laser scanning microscopy. *Biomech Model Mechanobiol* **11**, 461-473 (2012).
20. Biggs, L.C., Kim, C.S., Miroshnikova, Y.A. & Wickstrom, S.A. Mechanical Forces in the Skin: Roles in Tissue Architecture, Stability, and Function. *J Invest Dermatol* (2019).
21. Yuan, Y. *et al.* YAP1/TAZ-TEAD transcriptional networks maintain skin homeostasis by regulating cell proliferation and limiting KLF4 activity. *Nat Commun* **11**, 1472 (2020).
22. Candi, E., Schmidt, R. & Melino, G. The cornified envelope: a model of cell death in the skin. *Nat Rev Mol Cell Biol* **6**, 328-340 (2005).
23. Hatzfeld, M., Keil, R. & Magin, T.M. Desmosomes and Intermediate Filaments: Their Consequences for Tissue Mechanics. *Cold Spring Harb Perspect Biol* **9** (2017).